

# Autolabeling 3D Objects with Differentiable Rendering of SDF Shape Priors

Sergey Zakharov\*  
Technical University of Munich  
sergey.zakharov@tum.de

Wadim Kehl\*, Arjun Bhargava, Adrien Gaidon  
Toyota Research Institute  
firstname.lastname@tri.global

## Abstract

We present an automatic annotation pipeline to recover 9D cuboids and 3D shape from pre-trained off-the-shelf 2D detectors and sparse LIDAR data. Our autolabeling method solves this challenging ill-posed inverse problem by relying on learned shape priors and optimization of geometric and physical parameters. To that end, we propose a novel differentiable shape renderer over signed distance fields (SDF), which we leverage in combination with normalized object coordinate spaces (NOCS). Initially trained on synthetic data to predict shape and coordinates, our method uses these predictions for projective and geometrical alignment over real samples. We also propose a curriculum learning strategy, iteratively retraining on samples of increasing difficulty for subsequent self-improving annotation rounds. Our experiments on the KITTI3D dataset show that we can recover a substantial amount of accurate cuboids, and that these autolabels can be used to train 3D vehicle detectors with state-of-the-art results. We will make the code publicly available soon.

## 1. Introduction

Deep learning requires large labeled datasets to reach state-of-the-art performance. In the context of object detection for automated driving, 3D cuboids are the preferred annotation type since they allow for proper reasoning over all nine degrees of freedom (instance location, orientation, and metric extent). However, acquiring enough labels to train 3D object detectors is laborious and costly, as it mostly relies on a large number of human annotators. Current approaches towards scaling up annotation pipelines include better tooling, active learning, or a combination thereof [21, 14, 38, 24, 4]. These approaches often rely on heuristics and require humans in the loop to correct this semi-automatic labeling, especially for difficult edge cases.

In contrast, we propose to rely on differentiable ren-

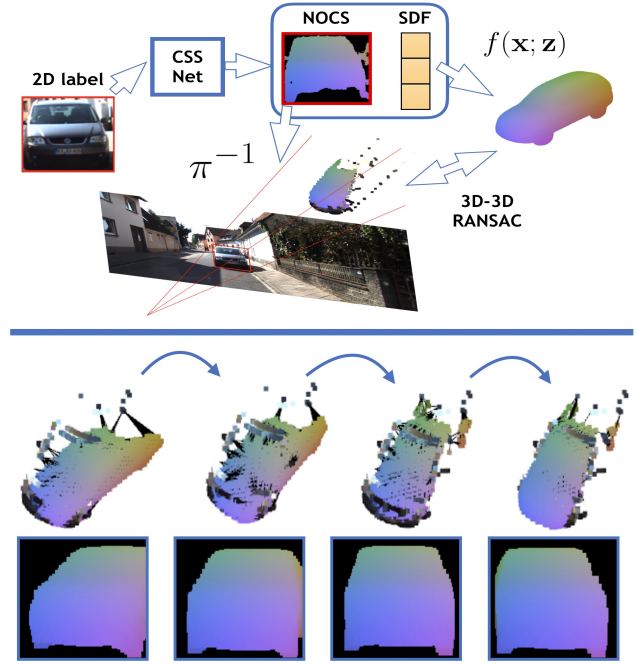


Figure 1: We propose a pipeline for 3D autolabeling of objects. Top: off-the-shelf 2D detections (boxes or instance masks) are fed to our Coordinate Shape Space (CSS) network to predict surface coordinates and a shape vector. We backproject the coordinates to LIDAR in a frustum and decode the shape vector into an object model. We establish 3D-3D correspondences between scene and model to estimate an initial affine transformation. Bottom: We iteratively refine the estimate via differentiable geometric and visual alignment.

dering of shape priors to recover metric scale, pose, and shape of vehicles in the wild. Our proposed 3D autolabeling pipeline requires only 2D detections (bounding boxes or instance masks) and sparse point clouds (ubiquitous in 3D robotic contexts). The detections themselves are produced by off-the-shelf 2D detectors. We show that differentiable visual alignment, a.k.a. 'analysis-by-synthesis' [41]

\* First co-authorship. This work resulted from an internship at TRI.

or ‘render-and-compare’ [19], is a powerful and principled approach to autolabeling for autonomous driving.

We present three novel contributions. First, we introduce the notion of a **Coordinate Shape Space (CSS)**, which couples Normalized Object Coordinates (NOCS) [37] with the DeepSDF framework [29]. This coupling allows us to reliably set object shapes into correspondence, facilitating *deformable shape matching*. Second, we present a way to differentiate DeepSDF with respect to its surface, thus introducing a novel **differentiable SDF renderer** for comparative scene analysis over a defined shape space. Our third contribution is a **curriculum learning-based autolabeling pipeline** of driving scenes. We refer to Figure 1 for an example optimization on the KITTI3D dataset [11].

Our pipeline starts with a CSS network trained to predict a 2D NOCS map as well as a shape vector from an image patch. To bootstrap an initial version, we train the network on synthetic data, for which we can easily acquire ground truth NOCS and shape vector targets, and apply augmentations to minimize the sim2real domain gap. Our autolabeling loop then consists of 1) leveraging 2D annotations to localize instances, 2) running the CSS network on an extracted patch, 3) reprojecting NOCS into the scene via LIDAR, 4) recovering an object model from the shape space, 5) computing an approximate pose via 3D-3D correspondences, and 6) running projective and geometric alignment for refinement. After processing all images, we harvest our recovered *autolabels* and retrain our CSS prediction network to gradually expand into the new domain. We then repeat the process to get increasingly better CSS predictions and, in turn, better autolabels. To avoid drifting with noisy autolabels, we employ a curriculum that focuses on easy samples first and increases the difficulty with each loop.

In summary, **our contributions** are (i) a novel, fully-differentiable renderer for signed distance fields that can traverse smooth shape spaces, (ii) a mixed synthetic/real curriculum framework that learns to predict shape and object coordinates on image patches, and (iii) a multi-modal optimization pipeline combining differentiable alignment over vision and geometry. We experimentally evaluate our approach on the KITTI3D dataset [11] to assess the quality of our labels. Overall, our results indicate that precisely recovering metric cuboids with structural, differentiable priors can be designed in an automated fashion. Furthermore, we will demonstrate that such cuboids can be leveraged for training surprisingly strong 3D object detection.

## 2. Related Work

In recent years, assisted labeling has gained much popularity since data growth outpaces our ability to label it manually. In [40] the authors use a 2D detector to seed 2D box annotations that are further refined by humans and report an increase of 60% in overall labeling speed. The authors

of [2] train a recurrent CNN to predict polygons on the image to accelerate semantic segmentation tasks. A follow-up work [24] further improves the system by predicting all polygon vertices simultaneously and allows for real-time interaction. In [21] the authors propose a 3D labeling interface that lets the users select spatial seeds from which to infer segmentation, 3D centroid, orientation, and extent via pretrained networks. [10] uses 2D labels to seed a LIDAR-based detector coupled with human annotation based on uncertainty. All mentioned works are active learning frameworks where a human is assisted by predictive models. Instead, we investigate how well an *automatic* pipeline with geometric verification can perform in this context.

Independently, much novel work has appeared in respect to differentiable rendering. The works [26, 17, 4] all present different ways to produce gradients for rasterization of triangle-based meshes. [25] presents a soft rasterizer approach where each pixel is softly assigned to each triangle in the mesh, followed by a softmax to emulate z-buffering. In contrast, [22] presents a path tracing approach towards differentiable rendering of triangle meshes.

More practically relevant, in [19, 28] the authors employ a learned shape space from PCA or CAEs to predict the shape of cars. Nonetheless, their shape space is either not differentiable end-to-end, or they use finite differences of local samples to approximate the gradient to avoid a complex back-propagation through the rasterizer. Differently to them, our differentiable rendering approach uses a shape space, derived from DeepSDF [29], which allows for back-propagation into a smooth shape manifold. Therefore, our method avoids the typical topology problems of related, mesh-based approaches.

DensePose [12] introduced a framework to densely map canonical 2D coordinates to human bodies. The inspiring works [16, 43, 44] show how to employ such coordinates with differentiable rendering in the wild to recover pose, shape, texture and even future motion for different entities from localized crops. [18] presents impressive results with a similar approach, trained with a cycle consistency and differentiable rendering. These methods allow for projective scene analysis up to scale and could not be immediately used for 3D automotive purposes.

Dense coordinates have recently been extended to 3D space. [42, 30, 23, 15, 32] apply such representations for monocular pose estimation of known CAD models. [37] learns to predict normalized coordinates (NOCS) for object categories in RGB data and recovers metric scale and pose with an additional depth map via 3D-3D correspondences.

In [8] the authors use stereo depth and run a detector to initialize instances which are further optimized for pose and shape via SDF priors. In a follow-up work [9] the authors extended the framework with temporal priors to simultaneously recover smooth shapes and pose trajectories.

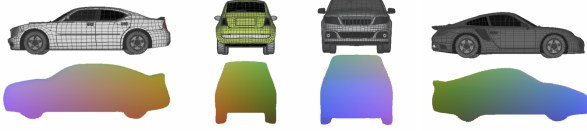


Figure 2: CSS representation. Top: Some car models from the PD dataset [1]. Bottom: The same cars in CSS representation: decoded shape vector  $\mathbf{z}$  colored with NOCS.

Slightly related, [36] explores 3D object completion via a shape space and LIDAR as weak supervision with a probabilistic formulation. Their work assumes correct localization and focuses solely on the reconstruction quality.

### 3. Methodology

We first discuss our shape space construction and the coupling into the CSS representation. Afterwards, we introduce our differentiable rendering approach tailored towards implicit surface representations. Eventually, the autolabeling pipeline is described in more detail.

#### 3.1. Coordinate Shape Space

As mentioned, we employ DeepSDF [29] to embed (watertight) car models into a joint, compact shape space representation with a single neural network. The idea is to transform input models into signed distance fields where each value signifies the distance to the closest surface, with positive and negative values representing exterior/interior area. Eventually, DeepSDF forms a shape space of implicit surfaces with a decoder  $f$  that can be queried at spatially-continuous 3D locations  $\mathbf{x} = \{x_1, \dots, x_N\}$  with a provided latent code  $\mathbf{z}$  to retrieve SDF values  $\mathbf{s} = \{s_1, \dots, s_N\}$ :

$$f(\mathbf{x}; \mathbf{z}) = \mathbf{s}. \quad (1)$$

In order to facilitate approximate *deformable shape matching*, we combine the shape space with NOCS [37] to form our Coordinate Shape Space (CSS). To this end, we resize our models to unit diameter and interpret the 3D coordinates of the 0-level set as dense surface descriptions.

To train  $f$ , we use a synthetic dataset provided by Parallel Domain [1] which comprises multiple CAD models of cars as well as rendered traffic scenes with ground truth labels. Other synthetic datasets (e.g. CARLA [7]) could have been used here as well. We trained on a subset of 11 models and with a shape dimensionality of 3. We follow the original DeepSDF training but project the latent vector onto the unit sphere after each iteration. In Figure 2 we depict some used models as well as their CSS representations.

#### 3.2. Differentiable SDF Rendering

An essential component of our autolabeling pipeline is the possibility to optimize objects in respect to pose, scale

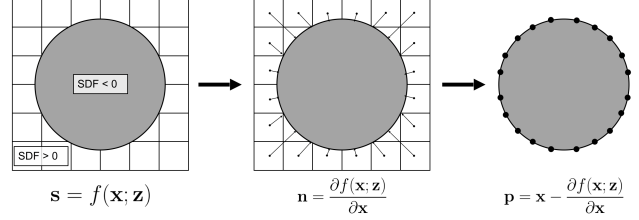


Figure 3: Surface projection. DeepSDF outputs signed values  $s$  for query locations  $\mathbf{x}$ . Normals  $\mathbf{n}$  can be computed analytically by a single backward pass. Given signed values and normals, we project the query locations onto object surface points  $\mathbf{p}$ . Only exterior points are visualized.

and shape. To this end, we propose, to the best of our knowledge, the first differentiable renderer for signed distance fields. Our renderer allows us to avoid mesh-related problems such as connectivity or intersections but necessitates a different way towards sampling the representation. In literature, the standard approach towards rendering implicit surfaces is either raytracing [6] or variants of Marching Cubes [27], but we present an alternative formulation that lends itself to back-propagation.

**Projection of 0-Isosurface** Provided with query points  $x_i$  and associated signed distance values  $s_i$ , we need a differentiable way to access the implicit surface. Simply selecting query points based on their distance values will not form a derivative with respect to the latent vector. Moreover, the regularly-sampled locations will always be only approximately on the surface. However, we use the fact that deriving the SDF with respect to its location yields the normal at this point, practically computed with a backward pass:

$$n_i = \frac{\partial f(x_i; \mathbf{z})}{\partial x_i}. \quad (2)$$

Since normals give us the direction to the closest surface and signed distance values provide the exact distance, we project the query location onto a 3D surface position  $p_i$ :

$$p_i = x_i - \frac{\partial f(x_i; \mathbf{z})}{\partial x_i} f(x_i; \mathbf{z}). \quad (3)$$

To get clean surface projections we disregard all points  $x_i$  outside a narrow band ( $|s_i| > 0.03$ ) of the surface. A schematic explanation can be seen in Figure 3. With this formulation, we can define derivatives at the  $p_i$  in respect to scale, pose or latent code.

**Surface Tangent Discs** In the domain of computer graphics the concept of surface elements (surfels) [33] is a well-established alternative to connected triangular primitives. Our differentiable SDF representation yields oriented points



Figure 4: Surface discs. Oriented tangent discs (right) represent the surface geometry much more accurately. We reduced spatial sampling and diameters for better emphasis.

and can be immediately used to render surface discs. To get a water-tight surface, we determine disk diameters large enough to close holes. In Figure 12 we show the difference between (oriented) surface tangent discs and billboard discs pointing straight at the camera.

We construct the surface discs with the following steps:

1. Given the normal of a projected point  $n_i = \frac{\partial f(p_i; \mathbf{z})}{\partial p_i}$ , estimate the 3D coordinates of the resulting tangent plane visible in the screen. The distance  $d$  of the plane to each 2D pixel  $(x, y)$  can be computed by solving a system of linear equations for the plane and camera projection, resulting in the following solution (we refer to the supplement for details):

$$d = \frac{n_i \cdot p_i}{n_i \cdot K^{-1} \cdot (x, y, 1)^T}, \quad (4)$$

where  $K^{-1}$  is the inverse camera matrix, followed by back-projection to get the final 3D plane coordinate:

$$P = K^{-1} \cdot (x \cdot d, y \cdot d, d)^T. \quad (5)$$

2. Estimate the distance between the plane vertex and surface point and clamp if larger than disc diameter:

$$M = \max(\text{diam} - \|p_i - P\|, 0) \quad (6)$$

To ensure water-tightness we compute the diameter from the query location density:  $\text{diam} = \min_{i \neq j} \|x_i - x_j\| \sqrt{3}$ . Computing above steps for each pixel yields a depth map  $\mathbf{D}_i$  and a tangential distance mask  $\mathbf{M}_i$  at point  $p_i$ .

**Rendering Function** In order to generate a final rendering we need a function to compose layers of 2D-projected discs onto the image plane. Similarly to [25], we combine colors from different point primitives based on their depth values. The closer the primitive is to the camera, the stronger its contribution. We use softmax to ensure that all primitive contributions sum up to 1 at each pixel. More specifically, the rendering function as:

$$\mathcal{I} = \sum_i \text{NOCs}(p_i) * w_i, \quad (7)$$

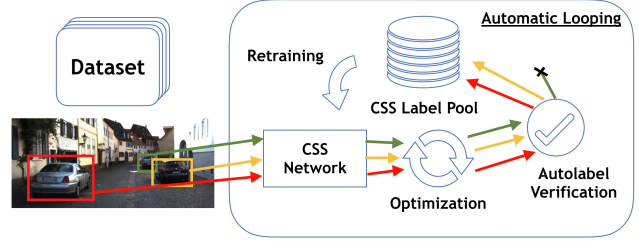


Figure 5: Automatic annotation pipeline. We fetch frames from the dataset and separately process each 2D annotation with our CSS network and differentiable optimization procedure. Afterwards, we run a verification to discard obviously wrong autolabels before harvesting them into our CSS label pool. Once all frames have been processed, we retrain our CSS network and begin the next loop over the dataset.

where  $\mathcal{I}$  is the resulting image,  $\text{NOCs}$  returns coordinate coloring, and  $w_i$  are the weighting masks that define the contribution of each disc:

$$w_i = \frac{\exp(-D_i \sigma M_i)}{\sum_j \exp(-D_j \sigma M_j)} M_i^{>0}, \quad (8)$$

where  $\sigma$  is a transparency constant with  $\sigma \rightarrow \infty$  being completely opaque as only the closest primitive is rendered. This formulation enables gradient flow from pixels to surface points and allows image-based optimization.

### 3.3. 3D Autolabeling Pipeline

The general idea of our autolabeling approach is to exploit weak labels and strong differentiable priors to recover labels of higher complexity. While this idea is generic, we focus specifically on cuboid autolabeling of driving scenes.

We present a schematic overview in Figure 14. We run multiple loops of our annotation pipeline. In the first loop, the CSS label pool solely consists of synthetic labels and the trained CSS network is therefore not well adapted to real imagery. The results are noisy NOCS predictions which are reliable only for *well-behaved* object instances in the scene. We therefore define a curriculum where we first focus on *easy* annotations and increase the difficulty over the next loops. We define the difficulty of an annotation by measuring the pixel sizes of the 2D label, the amount of intersection with other 2D labels, and whether the label touches the border of the image (often indicating object truncation). We establish thresholds for these criteria to define a curriculum of increasing difficulty.

**CSS Network** The network is derived from a ResNet18 and follows an encoder-decoder structure, processing  $128 \times 128$  input patches to output a NOCS map of the same size and 3D shape vector. Before the first annotation loop





Figure 6: Synthetic PD dataset. Top: Random RGB frame. Bottom: Some patches used for CSS training.

our CSS network must learn to infer 2D NOCS maps and shape vectors from patches. As mentioned, we bootstrap such a mapping from our synthetic PD dataset. In total we extract around 8k patches and, with access to the CAD models, create the necessary regression targets. We show some frames and training data in Figure 6 and provide additional information in the supplement.

### 3.3.1 Initialization & Optimization

We describe the process from Figure 1 in more detail. For a given patch we infer 2D NOCS map  $\mathcal{M}$  and shape vector  $\mathbf{z}$ . We decode  $\mathbf{z}$  into an SDF and retrieve the 3D surface points  $\mathbf{p} = \{p_1, \dots, p_n\}$  of the object model (as described in Section 3.2) in its local frame, for which compute the NOCS coordinates  $\mathbf{p}^c = \{p_1^c, \dots, p_n^c\}$ . We also project the 3D LIDAR points  $\mathbf{l} = \{l_1, \dots, l_k\}$  contained inside the frustum onto the patch and collect the corresponding NOCS coordinates  $\mathbf{l}^c$ . In order to estimate an initial pose and scale, we establish 3D-3D correspondences between  $\mathbf{p}$  and  $\mathbf{l}$ . We find for each  $p_i$  its nearest neighbor from NOCS distances:

$$j^* = \arg \min_j \|p_i^c - l_j^c\| \quad (9)$$

and keep it if  $\|p_i^c - l_{j^*}^c\| < 0.2$ . Finally, we run Procrustes [34] with RANSAC to estimate pose  $(R, t)$  and scale  $s$ .

From here, we start our differentiable optimization over complimentary 2D and 3D evidence. While projective 2D information provides strong cues for orientation and shape, 3D points allow reasoning over scale and translation. At every iteration we decode the current shape vector estimate  $\hat{\mathbf{z}}$ , extract surface points  $p_i$  and transform them with the current estimates for pose and scale:

$$\hat{p}_i = (\hat{R} \cdot \hat{s}) \cdot p_i + \hat{t}. \quad (10)$$

Given these surface model points in the scene frame, we compute our individual losses as follows:

**2D loss** We employ our differentiable SDF renderer to produce a rendering  $\mathcal{R}$  for which we seek maximum alignment with  $\mathcal{M}$ . Since our predicted  $\mathcal{M}$  can be noisy (especially in the first loop), minimizing dissimilarity  $\min \|\mathcal{M} - \mathcal{R}\|$  can yield unsatisfying solutions. Instead, we determine for each rendered spatial pixel  $r_i$  in  $\mathcal{R}$  the closest NOCS space neighbor in  $\mathcal{M}$ , named  $m_j$ , and set them in correspondence if their NOCS distance is below a threshold. To allow gradient flow, we use their spatial indices to resample the image locally. The loss is then the mean distance over all such correspondences  $C_{2D}$  in NOCS space:

$$loss_{2D} = \frac{1}{|C_{2D}|} \sum_{(i,j) \in C_{2D}} \|\mathcal{R}(r_i) - \mathcal{M}(m_j)\|. \quad (11)$$

**3D loss** For each  $\hat{p}_i$  we determine the nearest neighbor from  $\mathbf{l}$  and keep if it is closer than  $0.25m$ . Since our initializations are usually good, we avoid outliers in the optimization with such a tight threshold. The loss is then the mean distance over all correspondences  $C_{3D}$ :

$$loss_{3D} = \frac{1}{|C_{3D}|} \sum_{(i,j) \in C_{3D}} \|\hat{p}_i - l_j\|. \quad (12)$$

Altogether, the final criterion is the sum of both losses:

$$loss = loss_{2D} + loss_{3D}. \quad (13)$$

Since both loss terms work with similar magnitudes we did not observe the need for any additional balancing.

### 3.3.2 Verification & CSS Retraining

The optimization framework will unavoidably lead to wrong results at times and we need to ensure that we minimize the influence of badly-inferred autolabels. To this end, we enforce geometrical and projective verification to remove the most-offending autolabels. We measure the amount of LIDAR points which are in a narrow band ( $0.2m$ ) around the surface of the autolabel and reject if less than 60% are outside this band. Furthermore, we define a projective constraint where autolabels are rejected if the rendered mask's IoU with the provided 2D label falls below 70%.

All autolabels that survive the verification stage are harvested and added to the CSS label pool. After the first loop, we have a mixture of synthetic and real samples that are used to retrain and robustify our CSS network. Over multiple self-improving loops, we keep growing and retraining which in turn leads to better CSS predictions, better initializations and more accurate autolabels.

## 4. Experimental Evaluation

We evaluate our approach on the well-established KITTI3D dataset [11]. It consists of 7481 frames with

accompanied cuboid labels for the 'Car' category, which we focus on. We employ the most-widely used 3D metrics for driving datasets: BEV IoU and 3D IoU from KITTI3D as well as the distance-thresholded metric (NS) from NuScenes [3], which decouples location from scale and orientation. All three metrics evaluate Average Precision for matches at certain cutoffs, and we threshold BEV and 3D IoUs at 0.5 whereas NS is computed at distance cutoffs of 0.5m and 1m.

The KITTI3D metrics are often evaluated at a strict threshold of 0.7. After closer inspection, we observed that it is difficult to infer the correct cuboid size from tight surface fits. The KITTI3D cuboids have a varying amount of spatial padding and 3D detection methods learn these offsets. We therefore opted to relax the threshold to allow a fairer comparison to our tight cuboids. We refer to Figure 7 to see some examples of very good autolabel estimates of which some do not pass the 0.7 3D IoU criterion.

**Implementation Details** We use PyTorch [31] to implement the whole pipeline. For each 2D-labeled instance we run 50 iterations and use the ADAM optimizer for the pose variables with a learning rate of 0.03 whereas SGD is used for scale and shape with smaller learning rates (0.01 and 0.0005) and no momentum to avoid observed overshooting behavior. It takes around 6 seconds to autolabel one instance on a Titan V GPU, and one autolabeling loop takes 1-2 hours for all frames when parallelizing on 2 GPUs.

**Data Augmentation** Our synthetic bootstrapping must undergo many kinds of augmentation to allow for initial domain transfer. We use an extensive set of functions including random rotations up to  $10^\circ$ , horizontal flips, and random cropping. These not only help to dramatically expand the data size, but also help to explicitly cover cases of partial occlusion and truncation. Additionally, we change the brightness, contrast, and saturation of input patches. Moreover, since we have access to corresponding CAD models, we render surface normals and use Phong shading to generate geometrically-sensible relighting.

#### 4.1. Correctness of autolabels

The most important quantitative criterion is the actual correctness of our inferred cuboids. Although our method is fully automatic, we have access to KITTI3D 2D ground truth boxes and therefore evaluate two scenarios. Firstly, we ingest 2D boxes from KITTI3D for autolabeling and we use their defined criteria to determine whether an annotation is considered easy or moderate. Secondly, we use the detectron2 implementation [39] of Mask-RCNN [13] with a ResNeXt101 backbone trained on COCO to evaluate off-the-shelf object detectors for full automation. For the detection scenario we run separate experiments for boxes and

masks and we apply following difficulty criteria in spirit of KITTI3D: easy if label height  $> 40px$  and not touching other labels or image borders; moderate if height  $> 25px$  and not having an IoU  $> 0.30$  with any other label.

We present the results in Table 1. Unsurprisingly, the first loop with a purely synthetically-trained inference on easy real samples does not yield much difference between the three scenarios. All suffer from noisy CSS predictions and start from the same RANSAC initialization, although the detection-derived labels are tighter and slightly less influenced by CSS background noise. Overall, each scenario was able to retrieve close to **80% BEV AP** and around 60% in 3D AP over all easy samples. We conducted a second loop over the dataset with retrained CSS networks and see that the results for the easy samples have stabilized. Additionally, we see that we can recover around 60 BEV AP over all moderate samples. Noteworthy, our NS scores are quite high, signifying that most autolabels (more than 90%) are within one meter of the real location.

Furthermore, we evidently experience a sudden drop of around 20 points across all metrics for the harder samples. Since our method is reliant on 3D-3D Procrustes, we require a minimum set of inliers for proper solutions. We often observed that this makes correspondence finding difficult for occasional samples due to occlusion and distance, costing us recall.

Overall, we observe a rather fast diffusion into the target domain and that two loops are enough to stabilize the results. In Figure 8 we show the increasing quality of our NOCS predictions over multiple loops.

#### 4.2. Ablation

We want to investigate by how much the initial estimates from 3D-3D RANSAC benefit from our optimization. To this end, we use the easy ground truth boxes from KITTI3D and the synthetic CSS network to analyze the first annotation loop with the worst initialization. As can be seen from Table 3, the RANSAC baseline provides already quite good localization which is best captured by NS metrics (81.36% & 95.45%). Nonetheless, pose-optimized autolabels yield a significant jump in 3D IoU (41.85% vs. 63.42%) which suggests that we recovered substantially better rotations, given that NS scores are similar. When ablating over the other variables we see a rather mixed picture where certain metrics increase or decrease.

When ablating over the losses, we immediately see a drastic drop in the 3D metrics when optimizing only in 2D. Intuitively, our differentiable renderer aligns the data quite well in image space but both scale and translation are freely drifting. However, optimizing the 3D loss leads to strong spatial alignment. Nonetheless, optimizing the sum of both trades BEV AP (80.61 to 78.09) for 3D AP (60.92 to 63.53).

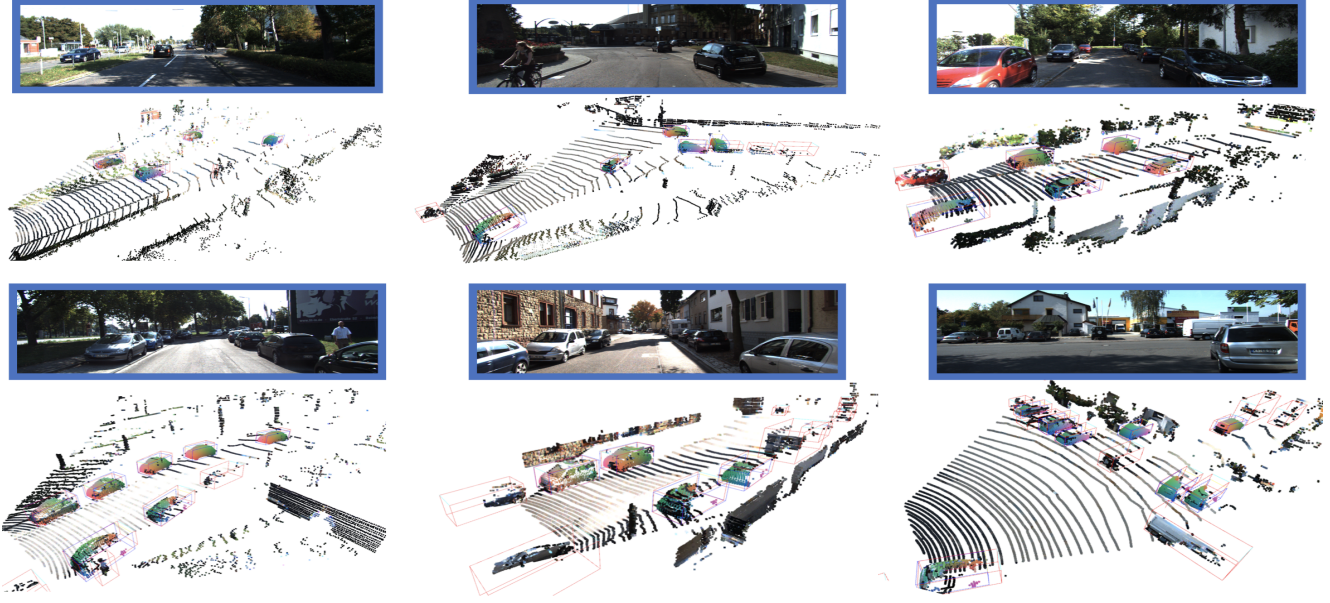


Figure 7: Qualitative results of our labeling pipeline. We draw the ground truth cuboids in red and our predictions in blue. Evidently, we can produce very tight fits that lead to cuboids of slightly different sizes compared the to the ground truth.

Loop	Diff.	KITTI GT				RCNN				MASK-RCNN			
		BEV@0.5	3D@0.5	NS@0.5	NS@1.0	BEV@0.5	3D@0.5	NS@0.5	NS@1.0	BEV@0.5	3D@0.5	NS@0.5	NS@1.0
1	E	78.09	63.53	85.59	95.58	78.45	63.71	85.85	95.62	78.46	63.69	86.27	95.76
2	E	77.84	62.25	82.40	90.84	80.57	60.11	86.05	94.62	80.70	63.96	86.52	94.31
	M	59.75	42.23	60.27	77.91	61.17	42.37	64.11	85.85	63.36	44.79	64.44	85.24

Table 1: Cuboid autolabel quality when using (a) - 2D ground truth boxes, (b) - RCNN detections, and (c) Mask-RCNN detections as CSS network input. We ran a total of two self-improving loops to slowly incorporate more labels into the pool.

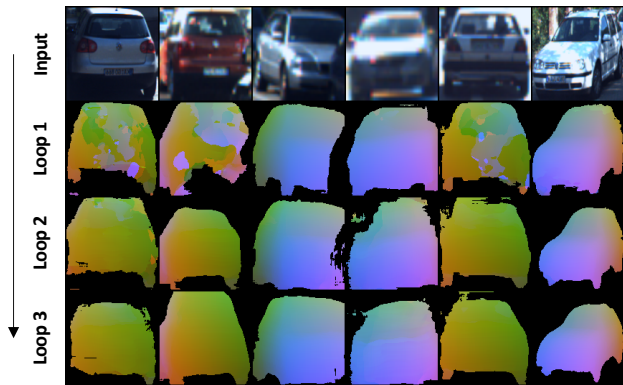


Figure 8: NOCS prediction quality of our network over consecutive loops for the same patch. Initially, the predictions are very noisy because of the synthetic domain gap. With each subsequent autolabeling loop the predictions tend to become more accurate overall.

### 4.3. 3D Object Detection

Since autolabels are usually not the final goal but rather a means to an end, we investigate the suitability of our labels for the 3D object detection task. We investigate the quality of our labels in both a traditional LIDAR based detection setting as well as in the purely monocular setting, based on several recent works that have achieved high quality results on the KITTI dataset [28, 35, 20].

We have reimplemented a version of the current state-of-the-art monocular detector MonoDIS [35] and ensured that we can reproduce the reported results. Additionally, we use the official implementation of PointPillars [20] which is a state-of-the-art LIDAR-only detector. To train MonoDIS, we follow the training schedule established in [35]. For PointPillars training, we accelerate the training by using 8 V100 GPUs and a batch size of 16. Accordingly, we scale the learning rate by a factor of 8. We evaluate our results on the MV3D train/val split [5]. When training on autolabels, we do not change any hyperparameters from the baseline protocols.



Method	2D AP @ 0.5/0.7		3D AP @ 0.5/0.7		BEV AP @ 0.5/0.7	
	Easy	Moderate	Easy	Moderate	Easy	Moderate
PointPillars [20] (Original Labels)	- / -	- / -	94.8 / 81.1	92.4 / 68.2	95.1 / 92.1	95.1 / 84.7
PointPillars [20] (Autolabels)	- / -	- / -	90.7 / 22.4	71.1 / 13.3	94.9 / 81.0	88.5 / 59.8
MonoDIS [35] (Original Labels)	96.1 / 95.5	92.6 / 86.5	45.7 / 11.0	32.9 / 7.1	52.4 / 17.7	37.2 / 11.9
MonoDIS [35] (Autolabels)	96.7 / 85.8	86.2 / 67.6	32.9 / 1.23	22.1 / 0.54	51.1 / 15.7	34.5 / 10.52

Table 2: We compare the performance of 3D object detectors trained on true KITTI labels vs. our autolabels. On the BEV metric, **the detectors trained on autolabels alone achieve results equal to the current state-of-the-art**. On the 3D AP metric, both autolabel trained detectors achieve competitive results at the IoU 0.5 threshold.

We present our numbers in Table 2 and some qualitative detections from autolabel-trained detectors in Figure 9.

Remarkably, on the BEV metric, both detectors trained *on autolabels alone* achieve competitive performance with the detectors trained on the true KITTI labels, at both the 0.5 and 0.7 IoU thresholds. This indicates that our autolabeling pipeline is capable of highly accurate localization of cuboids.

For the 3D AP metric, our results are in line with the conclusions displayed in Table 1. At the more tolerant IoU 0.5

threshold, our autolabel trained detectors perform within 70 – 90% of the true labels. Occasional missing detections and poor shape estimates do not significantly hurt overall performance.

As expected, at the IoU 0.7 threshold, the detector performance suffers. We argue that this is not due to poor predictions, but to the fact that KITTI labels are inflated relative to our estimated cuboids. Therefore, at the strictest threshold 3D IoU, we see a corresponding drop in precision for detectors trained on our “tighter” autolabels.

## 5. Conclusion

We presented a novel view on parametric 3D instance recovery in the wild by means of a self-improving autolabeling pipeline, purely bootstrapped from synthetic data and off-the-shelf detectors. Fundamental to our approach is the combination of dense surface coordinates with a shape space, and our contribution towards differentiable rendering of SDFs. We have shown that we can recover a substantial amount of cuboid labels with high precision from our pipeline and that these labels can be used to train 3D object detectors with close to state-of-the-art results. Future work includes investigating additional categories for parametric reconstruction, such as pedestrians or road surfaces.

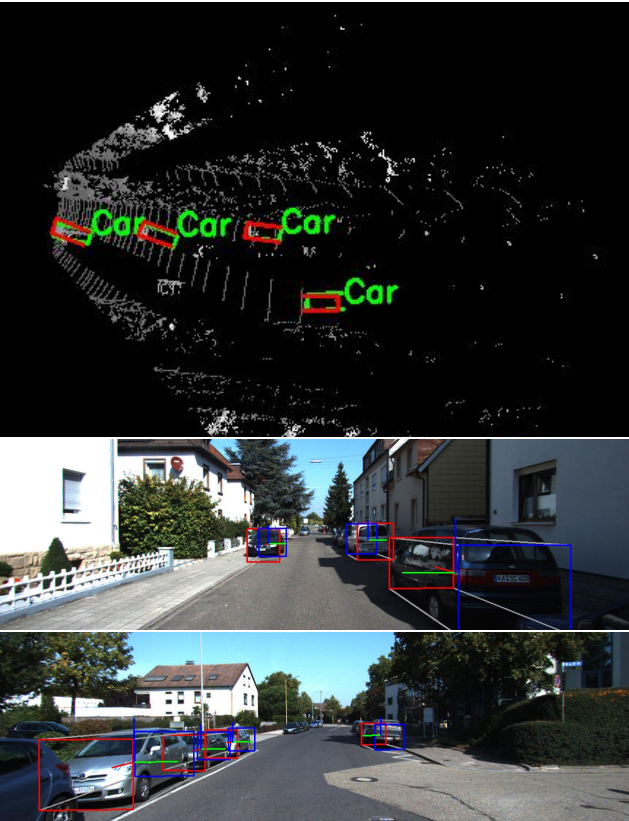


Figure 9: Detections from the autolabel-trained detectors. We draw local 3D frames to identify correct orientation.

Config	BEV@0.5	3D@0.5	NS@0.5	NS@1.0
RANSAC	77.00	41.85	81.36	95.45
$(R, t)$	77.19	63.42	86.20	95.53
$(R, t), s$	77.23	62.92	86.01	95.32
$(R, t), s, z$	78.09	63.53	85.59	95.58
2D loss	18.08	11.09	18.35	46.19
3D loss	80.61	60.92	85.63	95.49

Table 3: Ablation study over each optimization variable and each separate loss.



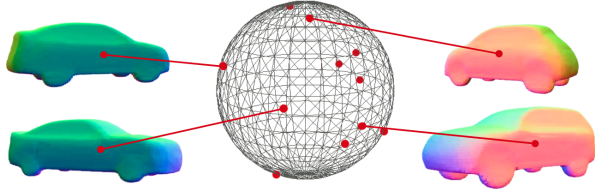


Figure 10: Visualization of the 3D latent vector space and the corresponding shapes after 0-isosurface projection.

## Supplementary Material

### A. DeepSDF

Our DeepSDF network is trained to cover a set of normalized predefined cars coming from the Parallel Domain (PD) dataset (visualized in Figure 11). Since we trained our latent shape vectors  $\mathbf{z}$  to be 3-dimensional, we can easily visualize their positions on the surface of a 3D sphere, as shown in Figure 10. Each red point represents a specific model shape embedded in the space.

### B. Data Generation

Given a set of ground truth poses with associated CAD models that we extract from our synthetic PD dataset (see Figure 13), we use our DeepSDF network and our differentiable renderer to project the models onto the screen. Instead of rendering the colors, we render the models' normalized coordinates (NOCS) represented as RGB channels (Figure 12c). Additionally we render the object normals (Figure 12b) that are subsequently used for 0-isosurface projection. Our augmentation module takes RGB crops (Figure 12a) and normal maps and applies 2D and 3D augmentations. 2D augmentations are based on the `torchvision.transforms` module operations and include random  $10^\circ$  rotations, horizontal flips, cropping, changes in brightness, contrast, and saturation. Moreover, normal maps provide us with local surface information that we use in conjunction with simple Phong shading. Thus, we

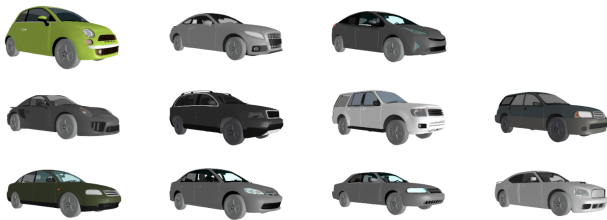


Figure 11: Cars from the PD dataset that were used to train our DeepSDF shape space.

can generate lighting based on different illumination types (namely ambient, diffusive, and specular) during training. Examples are shown in Figures 12d, 12e, 12f. Note how the bottom and top sides of the car change illumination between frames (e) and (f).

### C. Pipeline Components

The comprehensive representation of our pipeline is depicted in Figure 14. Below, we describe its main components in detail.

#### C.1. CSS Net

The architecture of our CSS net is visualized in Figure 14 and we use a ResNet18 backbone architecture. The decoders use bilinear interpolation as an upsampling operation rather than deconvolution to decrease the number of parameters and the required amount of computations. Each upsampling is followed by concatenation of the output feature map with the feature map from the previous level, and one convolutional layer. Since the CSS net is trained on synthetic data, it is initialized with ImageNet weights and the first five layers are frozen in order to prevent overfitting to peculiarities of the rendered data. Five heads of the CSS net are responsible for the output of U, V, and W channels of the NOCS as well as the object's mask and its latent vector, encoding its DeepSDF shape.

#### C.2. Pose Estimation Block

The pose estimation block (see initial conditions estimation in (Figure 14)) is based on 3D-3D correspondence estimation. The procedure is defined as follows: Our CSS net outputs normalized object coordinates (NOCS), mapping each RGB pixel to a 3D location on the object's surface. NOCS are backprojected onto the LIDAR frustum points using the provided camera parameters. Additionally, our network outputs a latent vector, which is then fed to

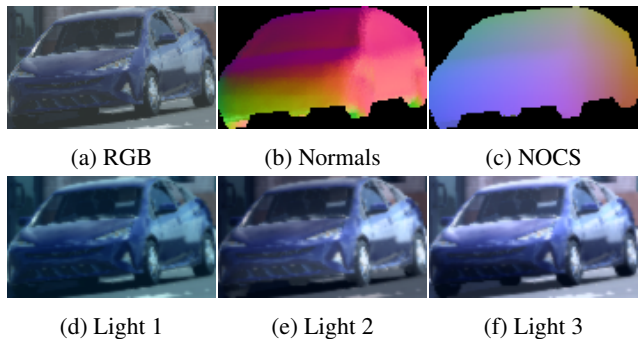


Figure 12: Data input modalities: (a) - input RGB image, (b) - rendered normal map, (c) - rendered NOCS. Light module outputs: (d, e, f).



Figure 13: Some example images from the PD dataset that we used for synthetic CSS training.

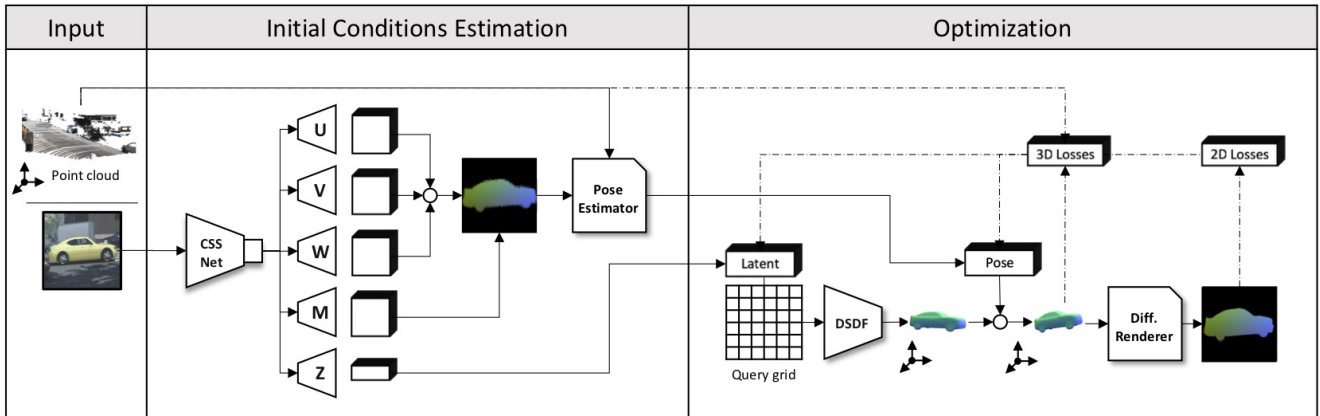


Figure 14: The core of the annotation pipeline. We fetch frames from the dataset and separately process each 2D annotation with our CSS network. The CSS net outputs 2D NOCS for each RGB input pixel, mask, and a latent shape vector. The latent vector is fed to our surface projection module to get a normalized car point cloud and the initial pose. The estimated pose transformation is then applied to the car and the 3D losses are computed. Our differentiable renderer is used to define losses in the dense 2D screen space.

the DeepSDF net and transformed to a surface point cloud using our 0-isosurface projection. Since our DeepSDF is trained to output normalized models placed at the origin, each point on the resulting model surface represents NOCS.

At this point, we are ready to proceed with pose estimation.

NOCS are used to establish correspondences between frustum points and model points. Backprojected frustum NOCS are compared to the predicted model coordinates,

and nearest neighbors for each frustum point are estimated. RANSAC is used for robust outlier rejection. At each iteration we take 4 random points ( $n$ ) from the set of the correspondences and feed them to the Procrustes algorithm, giving us initial estimates for the pose and scale of the model.

The following RANSAC parameters are used: the number of iterations  $k$  is based on a standard function of the desired probability of success  $p$  using a theoretical result:

$$k = \frac{\log(1 - p)}{\log(1 - w^n)}, \quad (14)$$

where  $w$  is the inlier probability and  $n$  are the independently selected data points. In our case  $p = 0.9$  and  $w = 0.7$ .

We use a threshold of 0.2m to estimate the inliers and choose the best fit. The final pose and scale are computed based on the inliers of the best fit.

### C.3. Optimization

Given the output of the CSS network and our pose initialization, we proceed to the optimization stage (see Figure 14). By concatenating the latent vector  $z$  with the query 3D grid  $x$  we form the input for our DeepSDF network. The DeepSDF net outputs SDF values for each query point on the grid, which we use for the 0-isosurface projection, providing us with a dense surface point cloud. The resulting point cloud is then transformed using the estimated pose and scale coming from the pose estimation module. The points that should not be visible from the given camera view are filtered using simple back-face culling, since surface normals have been already computed for 0-isosurface projection. At this stage, we are ready to apply 3D losses between the resulting transformed point cloud and the input LIDAR frustum points. The surface point cloud is also used as an input to our differentiable renderer, where we render NOCS as RGB and apply 2D losses between the CSS network's NOCS prediction and the renderer's output NOCS. The latent vector and the pose are then updated and the process is repeated until termination.

3D losses allow us to get a precise pose/shape alignment with the frustum points. However, it is often the case that only few points are available resulting in poor alignment results. 2D losses, on the other hand, allow for precise alignment in the screen space over dense pixels, but are unsuitable for 3D scale and translation optimization, and heavily rely on their initial estimates. The combination of the two losses gives us the best of both worlds: dense 2D alignment and robust scale/translation estimation.

## D. Surface Tangent Discs

Our surface tangent disc primitives formation requires solving a system of linear equations with a goal to compute the distance from the plane to each 2D pixel  $(x, y)$ :

$$\begin{cases} x' = (x - o_x) \frac{z'}{f_x} \\ y' = (y - o_y) \frac{z'}{f_y} \\ Ax' + By' + Cd - Ax'_0 - By'_0 - Cd_0 = 0 \end{cases} \quad (15)$$

The first 2 are the perspective projection equations and the third is a plane equation. If we solve the above system by a simple substitution, we get the following:

$$\begin{aligned} d \left( \frac{A(x - o_x)}{f_x} + \frac{B(y - o_y)}{f_y} + C \right) - Ax'_0 - By'_0 - Cd_0 &= 0 \longrightarrow \\ d &= \frac{Ax'_0 + By'_0 + Cd_0}{\left( \frac{A(x' - o_x)}{f_x} + \frac{B(y' - o_y)}{f_y} + C \right)} \\ &= \frac{n \cdot p_0}{n \cdot K^{-1}(x, y, 1)^T} \end{aligned} \quad (16)$$

As a result, we can retrieve a 3D plane position  $(x', y', d)$  for each 2D point  $(x, y)$  on the screen and form primitives based on 3D distances from 3D shape points.



## References

- [1] Parallel domain: Data generation for autonomy. <https://www.paralleldomain.com/>. 3
- [2] David Acuna, Huan Ling, Amlan Kar, and Sanja Fidler. Efficient interactive annotation of segmentation datasets with polygon-rnn++. In *CVPR*, 2018. 2
- [3] Holger Caesar, Varun Bankiti, Alex H. Lang, Sourabh Vora, Venice Erin Liong, Qiang Xu, Anush Krishnan, Yu Pan, Giancarlo Baldan, and Oscar Beijbom. nuscenes: A multimodal dataset for autonomous driving. *arXiv preprint arXiv:1903.11027*, 2019. 6
- [4] Wenzheng Chen, Jun Gao, Huan Ling, Edward J. Smith, Jaakko Lehtinen, Alec Jacobson, and Sanja Fidler. Learning to predict 3d objects with an interpolation-based differentiable renderer. In *NeurIPS*, 2019. 1, 2
- [5] Xiaozhi Chen, Huimin Ma, Ji Wan, Bo Li, and Tian Xia. Multi-view 3d object detection network for autonomous driving. In *VPR*, 2017. 7
- [6] Brian Curless and Marc Levoy. A volumetric method for building complex models from range images. In *SIGGRAPH*, 1996. 3
- [7] Alexey Dosovitskiy, German Ros, Felipe Codevilla, Antonio Lopez, and Vladlen Koltun. CARLA: An open urban driving simulator. In *CoRL*, 2017. 3
- [8] Francis Engelmann, Jörg Stückler, and Bastian Leibe. Joint object pose estimation and shape reconstruction in urban street scenes using 3D shape priors. In *GCPR*, 2016. 2
- [9] Francis Engelmann, Jörg Stückler, and Bastian Leibe. Samp: Shape and motion priors for 4d vehicle reconstruction. In *WACV*, 2017. 2
- [10] Di Feng, Xiao Wei, Lars Rosenbaum, Atsuto Maki, and Klaus Dietmayer. Deep active learning for efficient training of a lidar 3d object detector. In *IV*, 2019. 2
- [11] Andreas Geiger, Philip Lenz, and Raquel Urtasun. Are we ready for autonomous driving? the kitti vision benchmark suite. In *CVPR*, 2012. 2, 5
- [12] Rıza Alp Güler, Natalia Neverova, and Iasonas Kokkinos. Densepose: Dense human pose estimation in the wild. In *CVPR*, 2018. 2
- [13] Kaiming He, Georgia Gkioxari, Piotr Dollár, and Ross B. Girshick. Mask R-CNN. 2017. 6
- [14] Calvin Huang. Adding a dimension: Annotating 3d objects with 2d data. 2018. <https://scale.com/blog/3d-cuboids-annotations.1>
- [15] Omid Hosseini Jafari, Siva Karthik Mustikovela, Karl Pertsch, Eric Brachmann, and Carsten Rother. ipose: instance-aware 6d pose estimation of partly occluded objects. In *ACCV*, 2018. 2
- [16] Angjoo Kanazawa, Shubham Tulsiani, Alexei A. Efros, and Jitendra Malik. Learning category-specific mesh reconstruction from image collections. In *ECCV*, 2018. 2
- [17] Hiroharu Kato, Yoshitaka Ushiku, and Tatsuya Harada. Neural 3d mesh renderer. In *CVPR*, 2018. 2
- [18] Nilesh Kulkarni, Abhinav Gupta, and Shubham Tulsiani. Canonical surface mapping via geometric cycle consistency. 2019. 2
- [19] Abhijit Kundu, Yin Li, and James M. Rehg. 3d-rcnn: Instance-level 3d object reconstruction via render-and-compare. In *CVPR*, 2018. 2
- [20] Alex H. Lang, Sourabh Vora, Holger Caesar, Lubing Zhou, Jiong Yang, and Oscar Beijbom. Pointpillars: Fast encoders for object detection from point clouds. *CVPR*, 2019. 7, 8
- [21] Jungwook Lee, Sean Walsh, Ali Harakeh, and Steven Waslander. Leveraging pre-trained 3d object detection models for fast ground truth generation. In *ITSC*, 2018. 1, 2
- [22] Tzu-Mao Li, Miika Aittala, Frédo Durand, and Jaakko Lehtinen. Differentiable monte carlo ray tracing through edge sampling. 2018. 2
- [23] Zhigang Li, Gu Wang, and Xiangyang Ji. Cdpn: Coordinates-based disentangled pose network for real-time rgb-based 6-dof object pose estimation. In *CVPR*, 2019. 2
- [24] Huan Ling, Jun Gao, Amlan Kar, Wenzheng Chen, and Sanja Fidler. Fast interactive object annotation with curve-gcn. In *CVPR*, 2019. 1, 2
- [25] Shichen Liu, Tianye Li, Weikai Chen, and Hao Li. Soft rasterizer: A differentiable renderer for image-based 3d reasoning. *ICCV*, 2019. 2, 4
- [26] Matthew M. Loper and Michael J. Black. OpenDR: An approximate differentiable renderer. In *ECCV*, 2014. 2
- [27] William E. Lorensen and Harvey E. Cline. Marching cubes: A high resolution 3d surface construction algorithm. In *SIGGRAPH*, 1987. 3
- [28] Fabian Manhardt, Wadim Kehl, and Adrien Gaidon. Roi-10d: Monocular lifting of 2d detection to 6d pose and metric shape. In *CVPR*, 2019. 2, 7
- [29] Jeong Joon Park, Peter Florence, Julian Straub, Richard Newcombe, and Steven Lovegrove. Deepsdf: Learning continuous signed distance functions for shape representation. In *CVPR*, 2019. 2, 3
- [30] Kiru Park, Timothy Patten, and Markus Vincze. Pix2pose: Pixel-wise coordinate regression of objects for 6d pose estimation. In *CVPR*, 2019. 2
- [31] Adam Paszke, Sam Gross, Soumith Chintala, Gregory Chanan, Edward Yang, Zachary DeVito, Zeming Lin, Alban Desmaison, Luca Antiga, and Adam Lerer. Automatic differentiation in pytorch. In *NIPS-W*, 2017. 6
- [32] Sida Peng, Yuan Liu, Qixing Huang, Xiaowei Zhou, and Hujun Bao. Pvnnet: Pixel-wise voting network for 6dof pose estimation. In *CVPR*, 2019. 2
- [33] Hanspeter Pfister, Matthias Zwicker, Jeroen van Baar, and Markus Gross. Surfels: Surface elements as rendering primitives. In *SIGGRAPH*, 2000. 3
- [34] P.H. Schnemann. A generalized solution of the orthogonal procrustes problem. In *Psychometrika*, 1966. 5
- [35] Andrea Simonelli, Samuel Rota Buló, Lorenzo Porzi, Manuel Lopez-Antequera, and Peter Kontschieder. Disentangling monocular 3d object detection. In *ICCV*, 2019. 7, 8
- [36] David Stutz and Andreas Geiger. Learning 3d shape completion under weak supervision. *IJCV*, 2018. 3
- [37] He Wang, Srinath Sridhar, Jingwei Huang, Julien Valentin, Shuran Song, and Leonidas J. Guibas. Normalized object coordinate space for category-level 6d object pose and size estimation. In *CVPR*, 2019. 2, 3



- [38] Zian Wang, Huan Ling, David Acuna, Amlan Kar, and Sanja Fidler. Object instance annotation with deep extreme level set evolution. In *CVPR*, 2019. 1
- [39] Yuxin Wu, Alexander Kirillov, Francisco Massa, Wan-Yen Lo, and Ross Girshick. Detectron2. <https://github.com/facebookresearch/detectron2>, 2019. 6
- [40] Fisher Yu, Wenqi Xian, Yingying Chen, Fangchen Liu, Mike Liao, Vashisht Madhavan, and Trevor Darrell. Bdd100k: A diverse driving video database with scalable annotation tooling. 2018. 2
- [41] Alan Yuille and Daniel Kersten. Vision as bayesian inference: analysis by synthesis? *Trends in cognitive sciences*, 10(7):301–308, 2006. 1
- [42] Sergey Zakharov, Ivan Shugurov, and Slobodan Ilic. Dpod: Dense 6d pose object detector in rgb images. *ICCV*, 2019. 2
- [43] Jason Y. Zhang, Panna Felsen, Angjoo Kanazawa, and Jitendra Malik. Predicting 3d human dynamics from video. In *ICCV*, 2019. 2
- [44] Silvia Zuffi, Angjoo Kanazawa, Tanya Berger-Wolf, and Michael J. Black. Three-d safari: Learning to estimate zebra pose, shape, and texture from images ”in the wild”. In *ICCV*, 2019. 2